Shahrood University of Technology

Journal of Mining and Environment (JME)

Journal homepage: www.jme.shahroodut.ac.ir

Iranian Society of Mining Engineering (IRSME)

Engineering-Geological Controls on Rock Mass Fracturing and Mining-Induced Sinkhole Development in the Khandiza Polymetallic Deposit, Southern Uzbekistan

Agzamova Inobat[1], Abdurakhmanov Batir[2], Dadakhodjaeva Nasiba[3], Akhunjanov Alimjan[2], Elboy Kurbanov[2], Ibragimova Nodira[2], Esanova Zulfizar[4], Mukhiddin Juliev[1,5,6*]

1. Geology-prospecting and mining-metallurgy faculty, Tashkent State Technical University, Universitet 2, Tashkent, 100095, Uzbekistan
2. Institute of Hydrogeology and Engineering Geology, University of Geological Sciences, Mirzo Ulugbek district, Olimlar ko'chasi, 64, Tashkent, Uzbekistan
3. University of Geological Sciences, Mirzo Ulugbek district, Olimlar ko'chasi, 64, Tashkent, Uzbekistan
4. Department of Land Reclamation and Land Cadastre, Faculty of Irrigation Engineering, Karshi State Technical University, 225 Mustaqillik Avenue, Karshi, Kashkadarya, Uzbekistan
5. Institute of Fundamental and Applied Research, "TIIAME" National Research University, Kary-Niyaziy Str. 39, Tashkent 100000, Uzbekistan
6. Department of Civil Engineering and Architecture, Turin Polytechnic University in Tashkent, Little Ring Road Street 17, Tashkent 100095, Uzbekistan

Article Info

Received 13 September 2025
Received in Revised form 2 December 2025
Accepted 6 February 2026
Published online 6 February 2026

DOI: 10.22044/jme.2026.18111.3609

Keywords

Rock mass stability
Fault zones
Mining-induced sinkholes
Underground mining
Hydrogeology

Abstract

Underground extraction in fractured polymetallic rock masses may activate progressive deformation and surface collapse, particularly where faults, weak cover, groundwater pathways, and mining-induced disturbance interact. This study presents an evidence-constrained engineering-geological reconstruction of five collapse sinkholes that developed near the Khandiza polymetallic mine in southern Uzbekistan during 2016–2018. The analysis integrates underground and surface mapping records, fault-distance classes, laboratory strength data, archival time-dependent deformation observations, hydrogeological evidence, mine-development information, and repeated field measurements of the collapse area. The archival fracture-voidness coefficient (a comparative engineering index distinct from matrix porosity) increases from 1.5–3.0% at 15–20 m from major faults to 4.5–8.0% within the fault zone and its immediate influence belt, while uniaxial compressive strength decreases from 5–10 MPa to below 1–3 MPa. Across 28 laboratory shear-strength records, cohesion averages 16.83 ± 4.81 MPa (range 7.1–27.0 MPa) and the internal friction angle averages 42.05 ± 2.63° (range 36–47°); these are specimen-scale values and are not treated as in-situ rock-mass or fault-surface strength. The five sinkholes reached plan dimensions of approximately 12 × 13 to 60 × 80 m and visible depths of 6–40 m. Archived observations record a deformed area of about 0.8 km² and local crack widening or settlement rates of up to 1–2 mm/day. The strongest evidence for mining control is the non-backfilled caving environment, progressive roof collapse, the reported connection of Sinkhole 2 to the 1340 m mining horizon, and the spatial-temporal association between underground extraction and surface deformation. Groundwater and regional seismic shaking are treated as contributory or triggering factors rather than independently demonstrated causes because continuous pore-pressure, inflow, and site-acceleration records are unavailable. The resulting conceptual model is therefore mechanistic and semi-quantitative, not a calibrated predictive simulation.

1. Introduction

The progressive depletion of shallow mineral resources has led many underground operations to greater depths and more structurally complex rock masses. In these settings, excavation disrupts the natural stress equilibrium and reveals the engineering consequences of heterogeneity,

Corresponding author: mukhiddinjuliev@gmail.com (M. Juliev)

anisotropy, and discontinuity-controlled behaviour. Deep or locally highly stressed workings may experience brittle damage, squeezing, roof instability, convergence, rock falls, and delayed failure, while disturbances propagating through the overburden can ultimately affect the ground surface [1–5]. The engineering challenge is therefore not limited to the intact strength of individual rock types; it concerns the response of a rock mass composed of blocks, fractures, faults, altered zones, and groundwater pathways. Reliable assessment requires integrating geological observations with rock-mechanics parameters and mine-development history.

Discontinuities influence the scale and direction of rock-mass deformation by reducing effective strength, generating kinematic release surfaces, and redistributing stresses around excavations. The Q-system, Geological Strength Index, and related approaches provide useful frameworks for converting geological observations into engineering parameters, but their reliability depends on the quality of discontinuity characterization and recognition of major structures that cannot be represented by a single quality index [6–12]. Field and numerical studies show that fault location, fault-zone thickness, joint connectivity, and the contrast between intact and disturbed material can dominate the deformation pattern around underground openings [13,14]. In fractured ground, reinforcement may improve local confinement, but support design remains sensitive to the persistence and hydraulic condition of discontinuities [15]. These findings are particularly relevant to polymetallic deposits, where ore emplacement, hydrothermal alteration, and faulting often occur within the same structural corridors.

Recent work published in the Journal of Mining and Environment highlights the increasing emphasis on discontinuity-aware and uncertainty-aware stability assessment. Coupled finite-element and discrete-fracture-network modelling have demonstrated that explicit representation of natural fractures can alter the calculated support demand around underground openings [16]. Probabilistic tunnel analyses similarly show that deterministic parameter sets can underestimate displacement where rock-mass properties are spatially variable [17]. Physical and numerical investigations of reinforced supports, chain pillars, notched pillars, and friable ore bodies further emphasize that the geometry of weak zones and the mining sequence influence both load transfer and failure modes [18–22]. Research on caving-zone development provides a direct conceptual link between underground extraction, progressive upward failure, and surface deformation [23]. Groundwater studies in mining areas also underline that mining alters hydraulic gradients, water-rock interaction, and the movement of dissolved and suspended materials [24]. Together, these studies support an integrated approach to structure, mechanics, water, and extraction history rather than a single-factor interpretation.

Groundwater can accelerate deformation by increasing pore pressure, reducing effective stress, softening clay-rich infill, and enlarging connected flow paths. Conversely, excavation and blasting may create new hydraulic connections or drain previously isolated zones. These two-way interactions are commonly described as hydro-mechanical coupling [25]. Their long-term significance is amplified where rocks exhibit creep, stress corrosion, or delayed cracking. Laboratory and theoretical studies have shown that subcritical crack growth can produce time-dependent failure even when the sustained load remains below short-term peak strength [26–28]. Consequently, a rock mass that appears temporarily stable after excavation may continue to deteriorate under the combined effects of water, sustained stress, cyclic blasting, and progressive loss of confinement.

Mining-induced sinkholes and local collapse depressions are among the most hazardous manifestations of this progressive deterioration because they can develop rapidly at the surface after a prolonged and partly hidden subsurface evolution. Reviews of natural and human-induced sinkholes identify structural discontinuities, weak or soluble materials, groundwater movement, and anthropogenic voids as recurrent controls [29–33]. Mining-related deformation may involve a caved zone immediately above the opening, a fractured transition zone, and an upper zone of bending or discontinuous subsidence [34,35]. When overburden arching is insufficient, a collapse chimney can migrate upward until the surface is breached [36]. Satellite interferometry and UAV photogrammetry now provide effective tools for detecting distributed or localized pre-collapse deformation, although field mapping remains indispensable for interpreting the geological cause of the signal [37–40].

The Khandiza deposit lies within the western Tian Shan sector of the Central Asian Orogenic Belt, a region shaped by Paleozoic accretion, magmatism, deformation, and metallogenesis [41–46]. The deposit is developed in a mountain setting where ore-bearing structures, volcanic and

sedimentary units, hydrothermal alteration, and active underground extraction occur in close spatial association. Previous regional work has clarified the broad tectonic and metallogenic setting, but the engineering relationship among fault-zone fracturing, groundwater migration, rheological weakening, mine disturbance, and sinkhole development has not been presented as an integrated case study. This gap is significant because the observed surface collapses occur near a settlement and because continued mining advances toward deeper and structurally variable parts of the ore field.

Accordingly, the objectives of this study are to: (i) characterize the geological and structural controls on fracturing within the Khandiza rock mass; (ii) quantify the documented changes in engineering-geological properties with distance from faults; (iii) evaluate the available specimen-scale strength data and archival evidence of time-dependent weakening; (iv) reconstruct the chronology, geometry, spatial relationships, and measured precursory deformation of the Dibadom sinkholes; and (v) develop an evidence-constrained conceptual geomechanical model linking underground extraction, structural weakness, groundwater pathways, progressive caving, and surface breakthrough. The novelty lies not in introducing a new constitutive or numerical formulation, but in integrating five previously separate evidence streams at Khandiza: fault-distance deterioration data, laboratory strength records, mining and non-backfilling information, multi-year sinkhole chronology with measured deformation rates, and hydrogeological observations. The revised interpretation explicitly distinguishes direct observations from engineering interpretation and from hypotheses that remain unverified by site-specific monitoring.

2. Geological Setting of the Khandiza Deposit

2.1. Regional and structural setting

The Khandiza polymetallic deposit is situated in southeastern Uzbekistan within the South Uzbekistan ore district of the western Tian Shan. The regional framework forms part of the Central Asian Orogenic Belt, whose architecture records accretionary growth, arc-related magmatism, collision, and post-collisional deformation [41–46]. At the deposit scale, the ore field is characterized by a block-faulted structure. Ore bodies and hydrothermally altered zones are spatially associated with tectonic corridors containing faults, breccias, crushed rock, and dense fracture networks. These structures influence both ore localization and the subsequent mechanical response of the rock mass during excavation.

The Khandiza workings intersect sedimentary, volcanic, and intrusive units with contrasting competence. The main mapped materials include sandstones, siltstones, conglomerates, rhyolites, rhyolite porphyries, tuffaceous rocks, syenites and syenite porphyries, dolomites, schists, gneisses, and siliceous-carbonate rocks. Mesozoic-Cenozoic cover deposits consist of loessic and loam-rich materials that are comparatively weak and sensitive to water. Structural disturbance increases toward major faults, where the rock becomes fragmented, locally clay-infilled, and hydraulically connected. The block geometry, ore-body position, mine workings, and interpreted groundwater-flow paths are summarized in Figure 1.

2.2. Hydrogeological and mining conditions

Groundwater circulation in the ore field is primarily fracture-controlled. Relatively intact rock units have low matrix permeability, whereas faults, fracture intersections, and crushed zones form preferential flow paths. Springs and water inflows observed near structural zones confirm hydraulic communication between surface recharge, cover deposits, and deeper discontinuities. Mining has modified this system through drainage, excavation-induced unloading, blasting, and the creation of new voids and fractures. The resulting changes in gradient and saturation are important for clay-rich infill and altered rocks whose shear strength and creep resistance decrease after wetting.

Underground extraction has been conducted concurrently with exploration in parts of the Khandiza ore field. Archived mine and engineering-geological records indicate that the adopted extraction scheme did not provide complete backfilling of the mined-out space; natural roof caving, therefore, occurred above exhausted workings. This is an important site-specific constraint because steeply dipping faults and large fractures containing weak material can provide mechanically weakened pathways through which a caving zone may propagate upward. In the Dibadom sector, the overburden includes loess-like loams approximately 0.5–2.0 m thick over much of the slope and locally 10–12 m near its base, overlying fractured Jurassic sandstones, gravelites, and carbonaceous shales that dip about 20–25° toward the north-northwest. These archival observations strengthen the spatial link between the mined voids, structurally weakened bedrock, and the overlying collapse area, while not by themselves constituting a deterministic proof of the complete failure path.

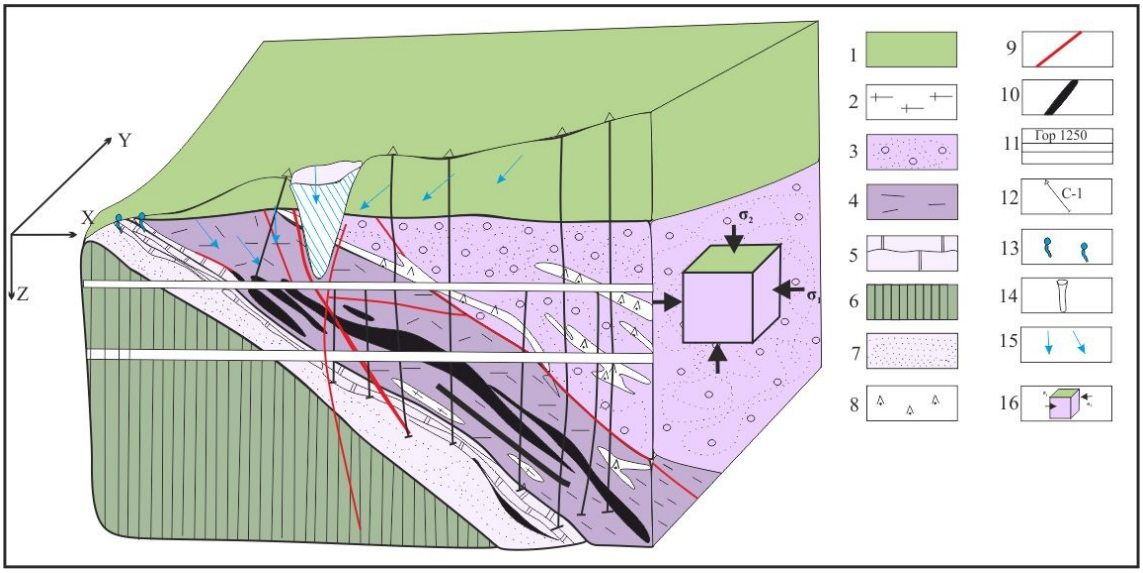

Figure 1. Structural block diagram of the Khandiza deposit showing the geological units, principal faults and fractures, ore bodies, underground workings, groundwater-flow directions, and the interpreted stress field. Legend: 1 - Mesozoic-Cenozoic deposits of the Vakhshivar Basin (sandstones, siltstones, loess soils, carbonaceous shales, gravelites), 2 - rhyolites, 3 - siltstones, sandstones, conglomerates, and rhyolites (Upper Subsuite), 4 - rhyolites (Middle Subsuite), 5 - dolomites, 6 - Khandiza Formation (schists and gneisses), 7 - Vakhshivar Formation (sandstones and tuffs), 8 - Podzhur Complex (diorite porphyries), 9 - fractures, 10 - ore body, 11 - underground mine workings, 12 - surface wells (a) and underground wells (b), 13 - springs, 14 - fault-zone cavity, 15 - direction of groundwater flow, 16 - maximum-stress field.

3. Materials and Methods

3.1. Field and structural investigations

The investigation is retrospective and combines archived engineering-geological mapping in underground workings with surface documentation of the Dibadom deformation area. The surviving discontinuity records describe orientation, spacing, persistence, aperture, roughness, infill, weathering, groundwater condition, and relationship to excavation geometry following the descriptive principles of the ISRM suggested method [47]. For the engineering comparison, observations were grouped into the fault-distance classes preserved in the original records: within the fault zone and up to 5 m from mapped faults, 5–15 m from faults, and 15–20 m from faults. The archive does not preserve the total number of scanlines, scanline lengths, or the complete set of individual discontinuity measurements; consequently, no new orientation-frequency statistics are claimed in this paper. Fault zones were distinguished from background jointing by persistence, fragmentation, brecciation/crushing, alteration or clay infill, and association with water inflow.

The parameter previously termed "fracture-voidness coefficient" has been revised throughout the manuscript to "fracture-voidness coefficient," which is the direct translation of the engineering index used in the archived Khandiza records. The original files report the index as a percentage and use it comparatively across fault-distance/strength classes, but they do not preserve the calculation equation, raw fracture-volume measurements, or a reproducible field protocol. It is therefore not interpreted as intact-rock matrix porosity and is not independently recalculated here; it is retained only as an archival comparative indicator of fracture-related void space. This limitation is explicitly considered when interpreting Table 1.

Surface investigations focused on the five documented Dibadom sinkholes and their precursor deformation. For each event, the archived records were reviewed for the first-observed date, elevation where available, initial and later plan dimensions, visible depth, crack geometry, settlement, and reported spatial relation to adjacent sinkholes, buildings, dry valleys, and underground workings. Repeated observations and photographs were used to reconstruct the progression from tensile cracking to subsidence and open collapse. Where direct depth measurement was unsafe, visible depth was kept separate from mine-reported underground connection. Relative distances among sinkholes are reported from the archived field notes; precise georeferenced coordinates for all five sinkholes were not preserved.

3.2. Laboratory strength database and archival time-dependent deformation evidence

The laboratory database contains 28 reported cohesion–friction records from multiple underground and borehole locations. The dataset comprises sandstone (n=3), syenite/syenite porphyry (n=2), siltstone/tuffaceous siltstone (n=2), rhyolite porphyry (n=6), rhyolite-dacite (n=3), tuffaceous/sericite tuffaceous rhyolite porphyry (n=7), siliceous-carbonate rock (n=4), and gneiss (n=1). Samples were obtained from boreholes, Adit No. 15, drifts, crosscuts, and working faces at the intervals listed in Table 2. The archive does not represent a statistically balanced sampling design: group sizes are unequal and some lithologies are represented by only one or two records. Descriptive statistics are therefore reported for the complete database, while lithology-specific values are interpreted cautiously. Uniaxial compressive strength and deformability were interpreted with reference to ISRM and ASTM procedures [48–50], and available shear-strength records were considered in the context of ISRM recommendations [51–53].

The cohesion and friction-angle values in Table 2 are laboratory/specimen-scale properties. They are not measurements of in-situ rock-mass strength and should not be transferred directly to a fault-controlled rock mass without scale, discontinuity, stress, and saturation corrections. The available archive contains no direct in-situ deformation-modulus tests and no dedicated direct-shear tests on saturated fault surfaces or fault gouge. Accordingly, the revised manuscript uses the laboratory data to demonstrate material variability only; it does not use them to calculate a rock-mass factor of safety or to claim quantitative fault stability.

Historical rheological records also contain empirical coefficients denoted β and χ and comparisons with Central Kyzylkum. Re-examination of the original source material showed that the archived dataset does not preserve a sufficiently reproducible constitutive definition, units, loading path, or calibration procedure for these coefficients. The previous quantitative β-χ table and the Central Kyzylkum comparison have therefore been removed from the revised manuscript. The only retained conclusion is qualitative and source-supported: selected water-sensitive lithologies showed greater time-dependent deformation after wetting with mine water. This observation is treated as supporting evidence for possible delayed weakening, not as a quantitative predictor of sinkhole formation.

3.3. Evidence classification and integrated interpretation

To avoid conflating measurement with interpretation, the revised analysis classifies evidence into three levels. Direct observations include mapped fault-distance classes, laboratory test results, mine records describing non-backfilled/caving conditions, sinkhole dates and dimensions, measured crack offsets and deformation rates, springs/water inflows, and repeated photographs. Engineering interpretations include upward migration of a caved zone and stress redistribution around mined openings, because these processes are consistent with the observed geometry and established mining mechanics but were not measured continuously at Khandiza [54]. Hypotheses include the magnitude of groundwater-induced pore-pressure change, fine-particle removal, and the dynamic contribution of regional earthquakes, because site-specific pore-pressure, turbidity/tracer, and strong-motion data are unavailable. Causal statements in the Results and Discussion are calibrated to these evidence levels.

The conceptual model is therefore an evidence-constrained mechanism reconstruction rather than a calibrated numerical simulation. A new three-dimensional hydro-mechanical model was considered during revision, but the available archive lacks the in-situ rock-mass modulus, saturated fault-surface shear parameters, site stress tensor, continuous pore-pressure history, blast vibration records, and georeferenced displacement time series required for defensible calibration. Introducing a numerical model without these inputs would create false precision; the missing parameters are instead identified explicitly as priorities for future work.

4. Results and Discussion

4.1. Fault-controlled fracturing and rock-mass deterioration

The archived engineering-geological data show a systematic deterioration of the reported rock-mass condition toward major faults. At 15-20 m from faults, slightly fractured rocks have fracture-voidness coefficients of 1.5-3.0% and reported uniaxial compressive strengths of 5-10 MPa. At 5-15 m, the coefficient rises to 3.0-4.5%, and strength decreases to 3-5 MPa. Within the fault zone and the immediate 0-5 m influence belt, the historical

classification contains two disturbed subcategories: 4.5-6.0% with UCS of 1-3 MPa and 6.0-8.0% with UCS below 1 MPa (Table 1). Because the archive does not preserve the original calculation protocol for the fracture-voidness coefficient, the numerical values are used only to document the relative deterioration across the original fault-distance classes rather than as an independently validated porosity measurement.

Table 1. Archived variation in engineering-geological rock-mass properties with distance from major fault zones at Khandiza.

Degree of fracturing	Position relative to faults	Fracture voidness (%)	Strength category	UCS (MPa)
Intensively fractured	Within fault zones and up to 5 m from faults	6.0-8.0	Very weak	<1
Intensively fractured	Within fault zones and up to 5 m from faults	4.5-6.0	Low-strength	1-3
Moderately fractured	5-15 m from faults	3.0-4.5	Strong	3-5
Slightly fractured	15-20 m from faults	1.5-3.0	High-strength	5-10

UCS - uniaxial compressive strength. The two intensively fractured rows are separate strength subcategories reported within the same ≤5 m fault-influence belt in the original records.

The results confirm that intact-rock properties alone are insufficient for stability assessment. A strong lithology intersected by a persistent fault may behave less favorably than a lower-strength but comparatively intact unit. This distinction is important because the spacing, persistence, and connectivity of discontinuities influence the equivalent deformation modulus and the scale of structurally controlled blocks [55,56]. Modern approaches that combine intact strength with structural information reach the same conclusion: rock-mass behaviour is governed by both material resistance and the geometry of its weaknesses [57].

4.2. Specimen-scale strength variability and time-dependent weakening

The 28-record laboratory shear-strength database shows substantial variability. Cohesion ranges from 7.1 to 27.0 MPa, with a mean of 16.83 MPa, a standard deviation of 4.81 MPa, and a median of 15.95 MPa. The internal friction angle ranges from 36° to 47°, with a mean of 42.05°, a standard deviation of 2.63°, and a median of 42°. Sandstones (n=3) have the highest group-average cohesion (24.33 MPa), whereas rhyolite-dacites (n=3) average 12.87 MPa; however, the unequal and small group sizes preclude inferential statistical comparison among lithologies. The wide within-group range, especially for rhyolite porphyry and tuffaceous rhyolite porphyry, is consistent with variable alteration and structural disturbance. These values characterize tested specimens, not the in-situ faulted rock mass.

Archival qualitative observations indicate that wetting by mine water increased time-dependent deformation in selected sandstones and clay-rich or altered rocks. Because the historical β and χ coefficients cannot be reconstructed from a documented constitutive equation or common set of units, they are not used in the revised quantitative interpretation. This change narrows the claim: time-dependent weakening is considered a plausible contributing process supported by historical wetting observations and by the general literature on subcritical crack growth and hydro-mechanical degradation, but its magnitude at the sinkhole scale remains unquantified.

4.3. Chronology and geometry of the Dibadom sinkholes

Five collapse sinkholes developed near the Dibadom settlement between February 2016 and May 2018. The first two appeared on 16 February 2016 near four residential buildings. Sinkhole 1 occurred at an elevation of approximately 1490-1495 m and measured about 12 × 13 m with a visible depth of 6–8 m. Sinkhole 2 occurred at approximately 1545 m and initially measured about 13 × 20 m. Direct surface depth measurement was unsafe; mine records reported a connection of approximately 155 m to the 1340 m mining horizon. During the following two months, continued collapse enlarged Sinkhole 2 to approximately 60 × 80 m with a visible depth of 25–30 m, while circular cracks 30–40 m long developed around it with vertical offsets of 0.2–0.3 m.

On 7 March 2017, an arcuate crack approximately 150–160 m long formed about 80 m northeast of Sinkhole 2 at an elevation of about 1592 m, with vertical settlement of 0.5–0.6 m. Sinkhole 3 formed on 13 August 2017 approximately 30 m northeast of Sinkhole 2, along a dry valley at about 1575 m elevation; it initially measured 20 × 15 m and 20–22 m deep and enlarged to about 30 × 50 m by 3 October 2017. Sinkhole 4 appeared on 16 January 2018 approximately 80 m north of the Sinkhole 2–3 area,

initially measuring about 10 × 15 m and about 10 m visible depth; ongoing caving increased its visible depth to approximately 30–40 m by late February. Sinkhole 5 formed in May 2018 on a gently sloping sector at approximately 1504–1508 m elevation, 2–3 m from a ruined house, and measured about 48 × 44 m with a visible depth of 18–20 m. Three to four rows of arcuate cracks formed 5–20 m from its southeastern margin, with individual crack lengths up to 45–50 m and vertical settlement of 5–10 cm. The spatial and temporal constraints are summarized in Table 3.

Table 2. Cohesion and internal friction angle of the tested lithological units in the Khandiza ore field (28 archival laboratory records).

Lithology	Sampling location/interval	Cohesion (MPa)	Friction angle (degrees)
Sandstone	Adit No. 15, R-360 m	27.0	42
Sandstone	Adit No. 15, R-140 m	26.5	45
Sandstone	Adit No. 15, R-5-8 m	19.5	44
Syenite	Borehole R-37-10, depth 60 m	25.0	44
Syenite porphyry	SP-44, Adit No. 15, 17-18 m	20.0	41
Siltstone	Borehole R-15-37 North, 25-30 m	14.9	42
Tuffaceous siltstone	Adit No. 15, Drift No. 1, Crosscut No. 38C	22.0	42
Rhyolite porphyry	Borehole R-15-2-41-C	9.6	47
Rhyolite porphyry	Face R-15-1-39	21.5	44
Rhyolite porphyry	Adit No. 15, R-600 m	20.3	40
Rhyolite porphyry	SP-37a, 54-56 m	15.0	38
Rhyolite porphyry	Borehole R-15-1-36-C, 98-99 m	14.1	44
Rhyolite porphyry	SP-93, 14.5-15.5 m	17.3	36
Rhyolite-dacite	Drift No. 1, 600-610 m	14.3	44
Rhyolite-dacite	Borehole R-15-1-36-C, 98-99 m	11.5	43
Rhyolite-dacite	Borehole R-15-1-36-C, 102-103 m	12.8	42
Tuffaceous rhyolite porphyry	Borehole R-15-2-42-S	7.1	44
Tuffaceous rhyolite porphyry	Crosscut No. 37 South	19.0	44
Tuffaceous rhyolite porphyry	PK-0+6	20.0	42
Sericite tuffaceous rhyolite porphyry	SP-37a, 17-18 m	15.7	37
Tuffaceous rhyolite porphyry	SP-44, 63-64 m	17.0	42
Tuffaceous rhyolite porphyry	SP-38, 270-271 m	15.0	40
Tuffaceous rhyolite porphyry	SP-44, 98-99 m	16.2	42
Siliceous-carbonate rock	Borehole R-38-C	14.2	42
Siliceous-carbonate rock	Borehole R-36-C	12.1	46
Siliceous-carbonate rock	Borehole R-39-C	13.0	42
Siliceous-carbonate rock	Borehole R-35-C	14.1	37.5
Gneiss	Adit No. 15, R-20 m	16.5	41

Table 3. Chronology, geometry, and relative spatial relationships of the five Dibadom sinkholes.

Sinkhole	Date / elevation	Dimensions / depth	Spatial relationship	Deformation / evidence notes
1	16 Feb 2016; 1490-1495 m	12 × 13 m; visible depth 6-8 m	Near four residential buildings	Direct field record.
2	16 Feb 2016; ~1545 m	Initial 13 × 20 m; enlarged to 60 × 80 m; visible depth 25-30 m	Same initial collapse sector; mine-reported ~155 m connection to the 1340 m horizon	Circular cracks 30-40 m; vertical offset 0.2-0.3 m; field + mine record.
3	13 Aug 2017; ~1575 m	20 × 15 m initially; 30 × 50 m by 3 Oct 2017; depth 20-22 m initially	~30 m NE of Sinkhole 2	A 150-160 m arcuate crack had formed ~80 m NE of Sinkhole 2 on 7 Mar 2017 with 0.5-0.6 m settlement.
4	16 Jan 2018; elevation not preserved	10 × 15 m; visible depth ~10 m initially and 30-40 m by late Feb 2018	~80 m north of the Sinkhole 2-3 area	Continued caving documented through late February 2018.
5	May 2018; 1504-1508 m	48 × 44 m; visible depth 18-20 m	2-3 m from a ruined house	Three-four arcuate crack rows 5-20 m from margin; settlement 5-10 cm; seismic triggering remains unverified.

Note: Relative positions are reproduced from archived field notes; complete georeferenced coordinates for all five sinkholes were not preserved.



(a) (b)

Figure 2. Collapse features near the Dibadom settlement: (a) open sinkhole developed above the mining area; (b) arcuate ground cracking and progressive deformation on the surrounding slope.

The chronology demonstrates a progressive rather than instantaneous failure process. Archived observations for the area around Sinkholes 2–4 describe a strongly deformed zone of approximately 0.8 km² between two dry valleys and local crack widening or settlement rates up to 1–2 mm/day. These measurements are not a continuous instrumented time series, but they provide quantitative field evidence of active surface deformation before and after sinkhole breakthrough. Together with the documented enlargement of Sinkholes 2–4, they support the use of crack-growth rate, settlement, and repeated geometry surveys as practical warning indicators [58]. The absence of continuous GNSS, levelling, InSAR, pore-pressure, and blast-vibration time series is addressed explicitly in Section 4.6.

4.4. Mining, groundwater, blasting, and seismic context

The causal link to mining is strongest where independent lines of site evidence converge. First, archived mine records state that mined-out spaces were not completely backfilled and that natural roof caving occurred. Second, the collapse area overlies active/exhausted underground workings within a faulted rock mass. Third, Sinkhole 2 was reported by the mine to connect approximately 155 m downward to the 1340 m horizon. Fourth, surface deformation progressed through cracking, settlement, enlargement, and repeated collapse rather than appearing as an isolated shallow depression. Blasting provides an additional disturbance capable of reactivating existing discontinuities, but no site-calibrated blast-stress or particle-velocity measurements were available. The generic blasting-stress schematic included in the submitted manuscript has therefore been removed because it did not add site-specific quantitative evidence.

Hydrogeological evidence is supportive but not quantitatively complete. Archived observations identify springs/water inflows near structural zones, fracture-controlled hydraulic pathways, and geophysical evidence interpreted as hydraulic communication between shallow water-bearing deposits and deeper discontinuities. However, no synchronized pore-pressure, hydraulic-head, discharge, tracer, turbidity, or suspended-sediment time series are available for the sinkhole episodes. Groundwater is therefore discussed as a plausible weakening and transport factor rather than a quantitatively demonstrated trigger. Likewise, the previously used term "suffosion" has been removed as an established mechanism: fine-particle removal remains a hypothesis because no direct sediment-loss measurements are available. The field archive also associated the formation of Sinkhole 5 with regional seismic activity on 9–10 May 2018. Independent earthquake data document an Mw 6.2 Hindu Kush event on 9 May 2018 (36.99°N, 71.37°E; depth about 111 km) [59]. Because no accelerogram or site-specific peak ground acceleration record exists at Khandiza, the temporal coincidence is treated only as a possible trigger acting on an already weakened rock mass, not as evidence that the earthquake caused the sinkhole.

4.5. Conceptual geomechanical model and engineering implications

The conceptual model in Figure 3 represents five connected stages constrained by the documented site geometry and chronology. First,

extraction occurs beneath a structurally disturbed rock mass containing faults, fractured ore-bearing zones, and lithological contacts. Second, removal of support and blasting redistribute stresses and may activate selected discontinuities. Third, local roof caving and time-dependent weakening enlarge the disturbed zone, while groundwater follows connected fractures. Fourth, an arch- or chimney-shaped collapse zone migrates upward, and the surface begins to crack and settle. Fifth, the residual bridge fails, and a collapse sinkhole forms; continued caving and lateral detachment may enlarge the surface opening. Quantitative constraints on this interpretation include the 0-5, 5-15, and 15-20 m fault-distance deterioration classes, the 0.5-12 m range of loess-like cover thickness reported in the collapse sector, bedrock dips of approximately 20-25° toward the N-NW, sinkhole plan dimensions up to 60 × 80 m, visible depths up to 40 m, and the mine-reported ~155 m connection for Sinkhole 2. These constraints narrow the plausible geometry but do not replace a calibrated three-dimensional model.

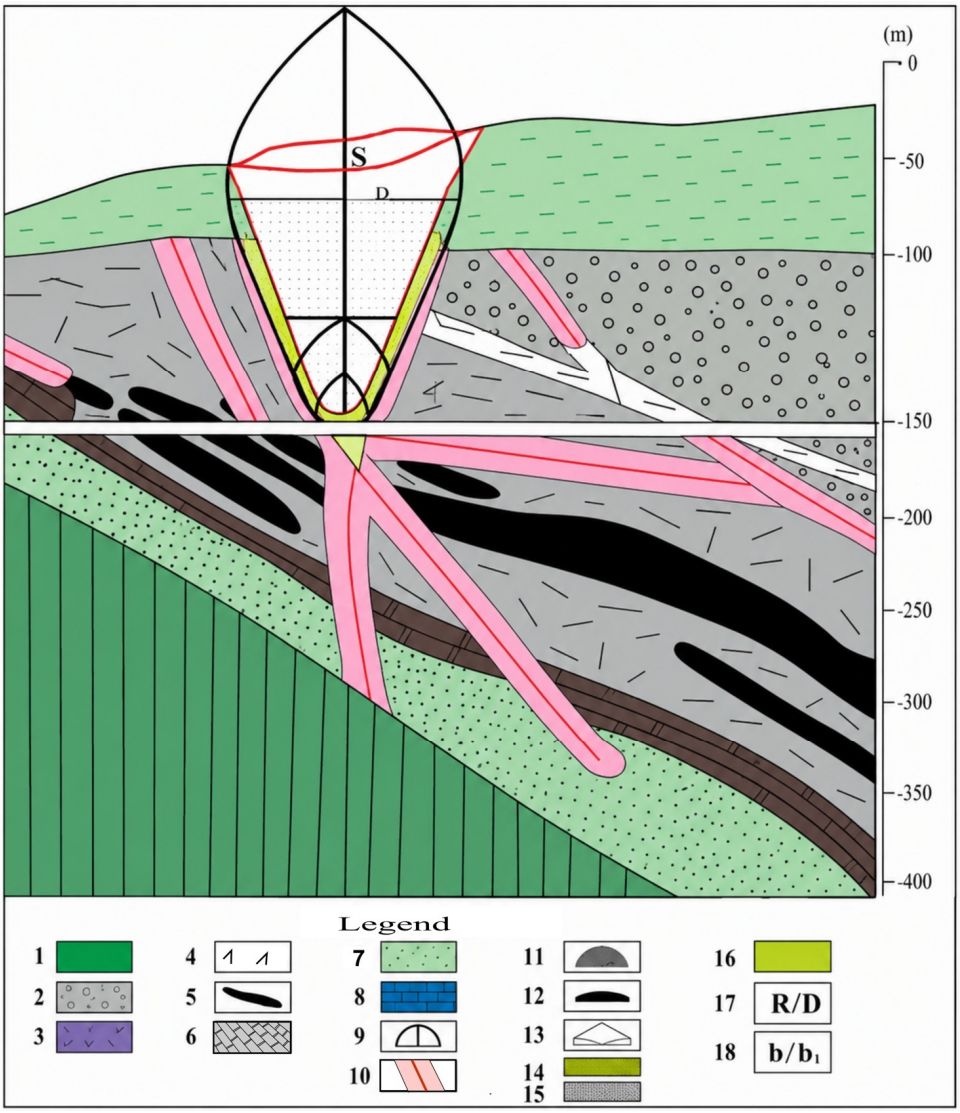

Figure 3. Conceptual scheme of collapse-sinkhole development in the Khandiza ore field. Legend: 1 – Mesozoic–Cenozoic deposits of the Vakhshivar Formation: sandstone, siltstone, carbonaceous shale, gravelite, sandy loam, and loam; 2 – siltstone, sandstone, conglomerate, and rhyolite of the Upper Subsuite; 3 – rhyolite of the Middle Subsuite; 4 – ore body; 5 – rock falls from underground mine workings; 6 – volume of the collapsed rock mass; 7 – caving-arch formation stage during the development of the collapse sinkhole; 8 – slip surface; 9 – density of the landslide mass; 10 – rock density along the slip surface; 11 – dolomite; 12 – sandstones and tuffs of the Lower Subsuite of the Vakhshivar Formation; 13 – collapse sinkhole; 14 – tectonic faults and fractures in the upper parts of the mountain ridges.

For mine planning, the model supports an evidence-overlap approach rather than a single deterministic threshold. Higher-concern sectors are those where active or exhausted workings without complete backfill underlie weak cover, major faults intersect the extraction zone, groundwater inflow or new springs occur, and surface cracking or settlement is accelerating. A practical monitoring system should combine routine underground fracture mapping, convergence measurements, water-inflow and piezometric records, controlled blast-vibration logs, surface crack gauges, levelling or GNSS benchmarks, and periodic UAV or InSAR surveys. Preventive measures may include modifying extraction beneath sensitive surface zones, backfilling where technically feasible, adapting blast energy near major faults, improving drainage control, and installing support promptly in weak lithologies [60].

Quantitative studies cited by Reviewer 2 provide useful benchmarks for the next stage of Khandiza analysis. Long-term goaf stability has been analysed with minimum-potential-energy formulations [61], the height of destressed/caved zones has been predicted using artificial neural networks and empirical data [62], long-term roof behavior has been evaluated using time-dependent caving concepts [63], and plastic-zone development around large underground openings has been assessed using calibrated numerical, fuzzy, and statistical models [64]. These studies reinforce the need for quantitative modelling, but they also depend on calibrated geometrical, mechanical, and/or monitoring inputs that are presently incomplete at Khandiza. The revised paper therefore uses them to frame the limits of the current conceptual reconstruction and the data requirements for a future 3-D hydro-mechanical model.

Table 4. Evidence matrix constraining the proposed Khandiza sinkhole mechanism.

Process / factor	Site evidence	Quantitative constraint	Interpretive status
Fault-zone weakening	Fault-distance classes; crushed/fractured zones; lower reported UCS near faults	Fracture-voidness coefficient 1.5-3.0% at 15-20 m, 3.0-4.5% at 5-15 m, 4.5-8.0% within ≤5 m; UCS 5-10 to <1-3 MPa	Direct archival association; index protocol incompletely documented
Mining void and roof caving	Incomplete backfilling; natural roof caving; collapse area above mine workings	Sinkhole 2 mine-reported connection ~155 m to 1340 m horizon	Strong site-specific support for mining contribution
Progressive surface deformation	Cracks, settlement, repeated enlargement, secondary collapse	~0.8 km² deformed area; local 1-2 mm/day crack widening/settlement; sinkholes up to 60 × 80 m	Direct field evidence of progressive failure
Groundwater	Springs/inflows and fracture-controlled hydraulic pathways; wetting-sensitive materials	No synchronized pore-pressure, head, or inflow-rate series	Plausible contributing factor; magnitude unquantified
Regional seismic shaking	Temporal association of Sinkhole 5 with May 2018 regional seismicity	Mw 6.2 Hindu Kush event on 9 May 2018; no site accelerogram	Possible trigger only; causality not demonstrated
Fine-particle removal	Hydraulically connected weak cover and fractures	No turbidity, sediment-loss, tracer, or grain-size transport measurements	Hypothesis; not treated as demonstrated suffosion

4.6. Strength of evidence and limitations

The principal limitation is the scale gap between laboratory specimens and the in-situ faulted rock mass. The reported cohesion, friction angle, and UCS values characterize tested materials and cannot represent rock-mass behavior without site-specific corrections for discontinuity, scale, stress, and water conditions. No direct in-situ deformation-modulus dataset, saturated fault-gouge direct-shear tests, or in-situ fault-surface cohesion/friction measurements were available. Therefore, the revised study does not compute a quantitative rock-mass factor of safety and does not use laboratory strength as proof of fault stability or sinkhole initiation. Dedicated testing of water-bearing fault infill and discontinuity surfaces is required before such calculations are defensible.

A second limitation is that the mechanism remains semi-quantitative rather than predictive. The historical dataset provides useful information on geometry, fault-distance classes, specimen strength, sinkhole chronology, and intermittent deformation measurements, but it lacks continuous pore pressure, hydraulic head, in-situ stress, blast vibration, three-dimensional mine-advance geometry, and georeferenced surface-displacement series. Consequently, the proposed sequence should be interpreted as an evidence-constrained conceptual mechanism. A fully quantitative, mechanism-based analysis will require a

coordinated monitoring program and a calibrated three-dimensional hydro-mechanical model. These limitations are now explicitly stated to prevent the conceptual model from being interpreted as a validated forward prediction.

Finally, several evidence streams have different confidence levels. Mining-induced caving and progressive surface deformation are directly supported by mine and field records; groundwater weakening is plausible but lacks event-scale hydraulic measurements; fine-particle removal is unverified; and the May 2018 earthquake can only be considered a possible trigger. This explicit separation of observation, interpretation, and hypothesis is maintained throughout the revised conclusions.

5. Conclusions

1. Archived fault-distance data demonstrate a consistent deterioration toward major faults: the fracture-voidness coefficient increases from 1.5–3.0% at 15–20 m to 4.5–8.0% within the ≤5 m fault-influence belt, while reported UCS decreases from 5–10 MPa to 1–3 MPa and <1 MPa in the most disturbed subcategory. Because the original voidness calculation protocol is unavailable, this is interpreted as a relative engineering trend.
2. The 28 laboratory shear-strength records yield cohesion of 16.83 ± 4.81 MPa (7.1–27.0 MPa) and an internal friction angle of 42.05 ± 2.63° (36–47°). These values quantify specimen-scale variability but are not representative of in-situ rock-mass or saturated fault-surface parameters.
3. The strongest quantitative field evidence is the 2016–2018 chronology of five sinkholes, which enlarged to as much as 60 × 80 m, with visible depths reaching 40 m, a deformed area of approximately 0.8 km², and local crack widening or settlement up to 1–2 mm/day. These observations demonstrate progressive surface deformation and identifiable precursors.
4. A mining contribution is supported by the non-backfilled caving environment, the position of the collapse area above underground workings, progressive roof/collapse records, and the mine-reported approximately 155 m connection of Sinkhole 2 to the 1340 m horizon. These converging observations support a mining-related interpretation more strongly than laboratory strength data alone.
5. Groundwater pathways and wetting-sensitive materials provide plausible support for hydro-mechanical weakening, but event-scale pore-pressure and flow data are absent; fine-particle removal is not directly demonstrated. The May 2018 regional earthquake is considered only as a possible trigger because no site strong-motion record exists.
6. The proposed five-stage model is an evidence-constrained conceptual reconstruction, not a calibrated predictive simulation. Its principal value is to organize the observed sequence from fault-controlled weakness and mining-induced caving to progressive cracking, settlement, and surface breakthrough.
7. Future work should prioritize quantitative scanline/televiewer fracture surveys, in-situ rock-mass deformability, saturated direct-shear testing of fault surfaces and gouge, continuous piezometric/inflow monitoring, blast-vibration measurements, GNSS/InSAR/UAV displacement time series, and calibration of a three-dimensional hydro-mechanical model against mine-advance and surface-deformation data.

References

[1]. *Rock Mechanics for underground mining*. (2004). Springer Netherlands.

[2]. Jing, L. (2003). A review of techniques, advances and outstanding issues in numerical modelling for rock mechanics and rock engineering. *International Journal of Rock Mechanics and Mining Sciences*, *40*(3), 283–353.

[3]. Diederichs, M. S., Kaiser, P. K., & Eberhardt, E. (2004). Damage initiation and propagation in hard rock during tunnelling and the influence of near-face stress rotation. *International Journal of Rock Mechanics and Mining Sciences*, *41*(5), 785–812.

[4]. Perras, M. A., & Diederichs, M. S. (2016). Predicting excavation damage zone depths in brittle rocks. *Journal of Rock Mechanics and Geotechnical Engineering*, *8*(1), 60–74.

[5]. Pan, P.-Z., Miao, S., Wu, Z., Feng, X.-T., & Shao, C. (2020). Laboratory Observation of Spalling Process Induced by Tangential Stress Concentration in Hard Rock Tunnel. *International Journal of Geomechanics*, *20*(3), 04020011.

[6]. Barton, N. (2002). Some new Q-value correlations to assist in site characterisation and tunnel design. *International Journal of Rock Mechanics and Mining Sciences*, *39*(2), 185–216.

[7]. Cai, M., Kaiser, P. K., Uno, H., Tasaka, Y., & Minami, M. (2004). Estimation of rock mass deformation modulus and strength of jointed hard rock masses using the GSI system. *International Journal of Rock Mechanics and Mining Sciences*, *41*(1), 3–19.

[8]. Hoek, E., & Marinos, P. (2007). A brief history of the development of the Hoek-Brown failure criterion. *Soils and Rocks*, *30*(2), 85–95.

[9]. Palmstrom, A. (2005). Measurements of and correlations between block size and rock quality designation (RQD). *Tunnelling and Underground Space Technology*, *20*(4), 362–377.

[10].Eberhardt, E. (2012). The Hoek–Brown Failure Criterion. *Rock Mechanics and Rock Engineering*, *45*(6), 981–988.

[11].Sonmez, H., & Ulusay, R. (1999). Modifications to the geological strength index (GSI) and their applicability to stability of slopes. *International Journal of Rock Mechanics and Mining Sciences*, *36*(6), 743–760.

[12].Marinos, V., Marinos, P., & Hoek, E. (2005). The geological strength index: Applications and limitations. *Bulletin of Engineering Geology and the Environment*, *64*(1), 55–65.

[13].Das, A. J., Mandal, P. K., Sahu, S. P., Kushwaha, A., Bhattacharjee, R., & Tewari, S. (2018). Evaluation of the Effect of Fault on the Stability of Underground Workings of Coal Mine through DEM and Statistical Analysis. *Journal of the Geological Society of India*, *92*(6), 732–742.

[14].Zhang, Z., Chen, F., Li, N., Swoboda, G., & Liu, N. (2017). Influence of fault on the surrounding rock stability of a tunnel: Location and thickness. *Tunnelling and Underground Space Technology*, *61*, 1–11.

[15].Wang, Q., Qin, Q., Jiang, B., Yu, H. C., Pan, R., & Li, S. C. (2019). Study and engineering application on the bolt-grouting reinforcement effect in underground engineering with fractured surrounding rock. *Tunnelling and Underground Space Technology*, *84*, 237–247.

[16].Noroozi, M., Rafiee, R., & Najafi, M. (2018). Stability analysis of support systems using a coupled FEM-DFN model (Case study: A diversion tunnel at Lorestan dam site, Iran). *Journal of Mining and Environment*, (Online First).

[17].Mazraehli, M., Zare, Sh., & Idris, M. (2021). Stochastic Stability Analysis of Tunnels Considering Randomness of Rock Mass Properties. *Journal of Mining and Environment*, *12*(4).

[18].Nehrii, S., Nehrii, T., Piskurska, H., Fesenko, E., Pavlov, Y., & Surzhenko, A. (2021). Substantiating Parameters of Reinforced Rock Supports. *Journal of Mining and Environment*, *12*(4).

[19].Abdollahi, M. S., Najafi, M., Yarahamdi Bafghi, A., & Rafiee, R. (2024). A New Method for Stability Analysis of Chain Pillar in Longwall Mining by using Coulmann Graphical Method. *Journal of Mining and Environment*, *15*(4).

[20].Rezaei, A., Sarfarazi, V., Babanouri, N., Omidi manesh, M., & Jahanmiri, S. (2023). Failure Mechanism of Rock Pillar Containing Two Edge Notches: Experimental Test and Numerical Simulation. *Journal of Mining and Environment*, *14*(3).

[21].Narwal, S., Deb, D., Islavath, S., & Samanta, G. (2024). Stability Assessment of Stoping Operations in Friable Ore Bodies under an Open Pit Mine using Strength-based Mining Sequence Factor. *Journal of Mining and Environment*, (Online First).

[22].Xia, Z.-Y., & Tan, Z.-Y. (2021). Study on Instability Mechanism of Extraction Structure under Undercut Space Based on Thin Plate Theory in Block Caving Method. *Shock and Vibration*, *2021*(1), 5548213.

[23].Alipenhani, B., Jalilian, M., Majdi, A., Bakhshandeh Amnieh, H., & Khosravi, M. H. (2024). Determination of the Caving Zone Height using Numerical and Physical Modeling based on the Undercutting Method Joint Dip and Spacing. *Journal of Mining and Environment*, *15*(4).

[24].Hembrom, S., & Kumari, N. (2026). Hydrogeochemical Characterization and Groundwater Quality Assessment in Mining Areas: A Review. *Journal of Mining and Environment*, *17*(1).

[25].Rutqvist, J., & Stephansson, O. (2003). The role of hydromechanical coupling in fractured rock engineering. *Hydrogeology Journal*, *11*(1), 7–40.

[26].Brantut, N., Heap, M. J., Meredith, P. G., & Baud, P. (2013). Time-dependent cracking and brittle creep in crustal rocks: A review. *Journal of Structural Geology*, *52*, 17–43.

[27].Borst, R. (2006). Modern Domain-based Discretization Methods for Damage and Fracture. *International Journal of Fracture*, *138*(1–4), 241–262.

[28].Damjanac, B., & Fairhurst, C. (2010). Evidence for a Long-Term Strength Threshold in Crystalline Rock. *Rock Mechanics and Rock Engineering*, *43*(5), 513–531.

[29].Gutiérrez, F., Parise, M., De Waele, J., & Jourde, H. (2014). A review on natural and human-induced geohazards and impacts in karst. *Earth-Science Reviews*, *138*, 61–88.

[30].Parise, M., & Lollino, P. (2011). A preliminary analysis of failure mechanisms in karst and man-made underground caves in Southern Italy. *Geomorphology*, *134*(1–2), 132–143.

[31].Galve, J. P., Gutiérrez, F., Remondo, J., Bonachea, J., Lucha, P., & Cendrero, A. (2009). Evaluating and comparing methods of sinkhole susceptibility mapping in the Ebro Valley evaporite karst (NE Spain). *Geomorphology*, *111*(3–4), 160–172.

[32].Parise, M. (2015). A procedure for evaluating the susceptibility to natural and anthropogenic sinkholes. *Georisk: Assessment and Management of Risk for Engineered Systems and Geohazards*, *9*(4), 272–285.

[33].Fiore, A., Fazio, N. L., Lollino, P., Luisi, M., Miccoli, M. N., Pagliarulo, R., Perrotti, M., Pisano, L., Spalluto, L., Vennari, C., Vessia, G., & Parise, M. (2018). Evaluating the susceptibility to anthropogenic sinkholes in Apulian calcarenites, southern Italy.

Geological Society, London, Special Publications, *466*(1), 381–396.

[34].Zhang, Q., Guo, J., Lu, X., Ding, K., Yuan, R., & Wang, D. (2024). Simulation and On-Site Detection of the Failure Characteristics of Overlying Strata under the Mining Disturbance of Coal Seams with Thin Bedrock and Thick Alluvium. *Sensors*, *24*(6), 1748.

[35].Zhou, Z., Cao, J., Lai, L., Zhou, J., & Xu, M. (2023). Determination of the Caving Zone and Fracture Zone Heights by Using the LK-Means Algorithm. *Advances in Civil Engineering*, *2023*, 1–7.

[36].Vyazmensky, A., Elmo, D., & Stead, D. (2010). Role of Rock Mass Fabric and Faulting in the Development of Block Caving Induced Surface Subsidence. *Rock Mechanics and Rock Engineering*, *43*(5), 533–556.

[37].Guzy, A., & Malinowska, A. (2020). State of the Art and Recent Advancements in the Modelling of Land Subsidence Induced by Groundwater Withdrawal. *Water*, *12*(7), 2051.

[38].Qin, Y., Xiao, X., Dong, J., Zhang, G., Shimada, M., Liu, J., Li, C., Kou, W., & Moore, B. (2015). Forest cover maps of China in 2010 from multiple approaches and data sources: PALSAR, Landsat, MODIS, FRA, and NFI. *ISPRS Journal of Photogrammetry and Remote Sensing*, *109*, 1–16.

[39].Wasowski, J., & Bovenga, F. (2014). Investigating landslides and unstable slopes with satellite Multi Temporal Interferometry: Current issues and future perspectives. *Engineering Geology*, *174*, 103–138.

[40].Ćwiąkała, P., Gruszczyński, W., Stoch, T., Puniach, E., Mrocheń, D., Matwij, W., Matwij, K., Nędzka, M., Sopata, P., & Wójcik, A. (2020). UAV Applications for Determination of Land Deformations Caused by Underground Mining. *Remote Sensing*, *12*(11), 1733.

[41].Yakubchuk, A. (2004). Architecture and mineral deposit settings of the Altaid orogenic collage: A revised model. *Journal of Asian Earth Sciences*, *23*(5), 761–779.

[42].Windley, B. F., Alexeiev, D., Xiao, W., Kröner, A., & Badarch, G. (2007). Tectonic models for accretion of the Central Asian Orogenic Belt. *Journal of the Geological Society*, *164*(1), 31–47.

[43].Xiao, W., Windley, B. F., Allen, M. B., & Han, C. (2013). Paleozoic multiple accretionary and collisional tectonics of the Chinese Tianshan orogenic collage. *Gondwana Research*, *23*(4), 1316–1341.

[44].Yakubchuk, A. (2017). Evolution of the Central Asian Orogenic Supercollage since Late Neoproterozoic revised again. *Gondwana Research*, *47*, 372–398.

[45].Safonova, I., Seltmann, R., Kröner, A., Gladkochub, D., Schulmann, K., Xiao, W., Kim, J., Komiya, T., & Sun, M. (2011). A new concept of continental construction in the Central Asian Orogenic Belt. *Episodes*, *34*(3), 186–196.

[46].Xiao, W., Windley, B. F., Sun, S., Li, J., Huang, B., Han, C., Yuan, C., Sun, M., & Chen, H. (2015). A Tale of Amalgamation of Three Permo-Triassic Collage Systems in Central Asia: Oroclines, Sutures, and Terminal Accretion. *Annual Review of Earth and Planetary Sciences*, *43*(1), 477–507.

[47].International society for rock mechanics commission on standardization of laboratory and field tests. (1978). *International Journal of Rock Mechanics and Mining Sciences & Geomechanics Abstracts*, *15*(6), 319–368.

[48].Bieniawski, Z. T., & Bernede, M. J. (1979). Suggested methods for determining the uniaxial compressive strength and deformability of rock materials. *International Journal of Rock Mechanics and Mining Sciences & Geomechanics Abstracts*, *16*(2), 138–140.

[49].Muralha, J., Grasselli, G., Tatone, B., Blümel, M., Chryssanthakis, P., & Yujing, J. (2014). ISRM Suggested Method for Laboratory Determination of the Shear Strength of Rock Joints: Revised Version. *Rock Mechanics and Rock Engineering*, *47*(1), 291–302.

[50].D18 Committee. (n.d.). *Test Methods for Compressive Strength and Elastic Moduli of Intact Rock Core Specimens under Varying States of Stress and Temperatures*. ASTM International.

[51].C18 Committee. (n.d.). *Test Methods for Absorption and Bulk Specific Gravity of Dimension Stone*. ASTM International. https://doi.org/10.1520/C0097_C0097M-18

[52].Zhang, L., & Einstein, H. H. (2000). Estimating the intensity of rock discontinuities. *International Journal of Rock Mechanics and Mining Sciences*, *37*(5), 819–837.

[53].Zhang, L., & Einstein, H. H. (2004). Using RQD to estimate the deformation modulus of rock masses. *International Journal of Rock Mechanics and Mining Sciences*, *41*(2), 337–341.

[54].Lou, J., Gao, F., Yang, J., Ren, Y., Li, J., Wang, X., & Yang, L. (2021). Characteristics of evolution of mining-induced stress field in the longwall panel: Insights from physical modeling. *International Journal of Coal Science & Technology*, *8*(5), 938–955.

[55].Yao, Y., Lu, N., Yang, Y., Cao, Y., & Yu, H.-S. (2019). Study of long-termed displacements of a tunnel boring machine during its stoppage. *Tunnelling and Underground Space Technology*, *84*, 432–439.

[56].Meng, F., Wong, L. N. Y., & Zhou, H. (2021). Rock brittleness indices and their applications to different fields of rock engineering: A review. *Journal of Rock Mechanics and Geotechnical Engineering*, *13*(1), 221–247.

[57].Martini, C. D., Read, R. S., & Martino, J. B. (1997). Observations of brittle failure around a circular test tunnel. *International Journal of Rock Mechanics and Mining Sciences*, *34*(7), 1065–1073.

[58].Strzałkowski, P. (2026). Proposal for Preparing Forecasts of Sinkhole Formation. *Pure and Applied Geophysics*, *183*(3), 1091–1105.

[59].United States Geological Survey (2018). (2026, September 25). *M 6.2—36 km NW of Ishkashim, Tajikistan, 9 May 2018, 10:41:46 UTC, depth 111 km, event us1000e19e* [U.S. Geological Survey Earthquake Hazards Program].

[60].Xing, Y., Kulatilake, P. H. S. W., & Sandbak, L. A. (2018). Effect of rock mass and discontinuity mechanical properties and delayed rock supporting on tunnel stability in an underground mine. *Engineering Geology*, *238*, 62–75.

[61].Rezaei, M. (2018). Long-term stability analysis of goaf area in longwall mining using minimum potential energy theory. *Journal of Mining and Environment*, *9*(1).

[62].Majdi, A. and Rezaei, M. (2013). (n.d.). *Application of artificial neural networks for predicting the height of destressed zone above the mined panel in longwall coal mining*. Proceedings of the 47th U.S. Rock Mechanics/Geomechanics Symposium, San Francisco, California, USA, ARMA 13-605.

[63].Mohammad, R., Abbas, M., Mohammad, F. H., & Iraj, N. (2018). Study of the roof behavior in longwall gob in long-term condition. *Journal of Geology and Mining Research*, *10*(2), 15–27.

[64].Rezaei, M., & Rajabi, M. (2021). Assessment of plastic zones surrounding the power station cavern using numerical, fuzzy and statistical models. *Engineering with Computers*, *37*(2), 1499–1518.

انجمن مهندسی معدن ایران
نشریه مهندسی معدن و محیط زیست
نشانی نشریه: www.jme.shahroodut.ac.ir
دانشگاه صنعتی شاهرود

کنترل‌های زمین‌شناسی مهندسی بر شکستگی توده سنگ و ایجاد فروچاله‌های ناشی از فعالیت‌های معدنی در کانسار پلی‌متالیک خندی‌زا، جنوب ازبکستان

آگزاموا اینوبات[۱]، عبدالرخمانوف باتیر[۲]، داداخجاوا نصیبا[۳]، آخونجانف علیمجان[۲]، البوی کوربانوف[۲]، ایبراگیموا نودیرا[۲]، اسانوا زولفیزار[۴]، مخدین جولیف[۱،۵،۶*]

۱. دانشکده زمین‌شناسی-اکتشاف و معدن-متالورژی، دانشگاه فنی دولتی تاشکند، خیابان اونیورسیتت ۲، تاشکند، ۱۰۰۰۹۵، ازبکستان
۲. موسسه هیدروژئولوژی و زمین‌شناسی مهندسی، دانشگاه علوم زمین‌شناسی، منطقه میرزا الغ‌بیگ، خیابان اولیم‌لار، پلاک ۶۴، تاشکند، ازبکستان
۳. دانشگاه علوم زمین‌شناسی، منطقه میرزا الغ‌بیگ، خیابان اولیم‌لار، پلاک ۶۴، تاشکند، ازبکستان
۴. گروه احیای اراضی و کاداستر اراضی، دانشکده مهندسی آبیاری، دانشگاه فنی دولتی قارشی، خیابان موستاکیلیک، پلاک ۲۲۵، قارشی، قشقه‌دریا، ازبکستان
۵. موسسه تحقیقات بنیادی و کاربردی، دانشگاه تحقیقاتی ملی«TIIAME» ، خیابان کاری-نیازی، پلاک ۳۹، تاشکند ۱۰۰۰۰۰، ازبکستان
۶. گروه مهندسی عمران و معماری، دانشگاه پلی‌تکنیک تورین در تاشکند، خیابان لیتل رینگ رود (Little Ring Road)، پلاک ۱۷، تاشکند ۱۰۰۰۹۵، ازبکستان

اطلاعات مقاله

تاریخ ارسال: ۲۰۲۶/۰۸/۰۶
تاریخ داوری: ۲۰۲۶/۰۹/۲۵
تاریخ پذیرش: ۲۰۲۶/۱۱/۰۱

DOI: 10.22044/jme.2026.18111.3609

کلمات کلیدی

پایداری توده سنگ
زون‌های گسلی
فروچاله‌های ناشی از فعالیت‌های معدنی
معدن‌کاری زیرزمینی
هیدروژئولوژی

چکیده

استخراج زیرزمینی در توده‌های سنگی پلی‌متالیک شکسته ممکن است تغییر شکل پیشرونده و فروپاشی سطحی را فعال کند، به ویژه در مواردی که گسل‌ها، پوشش ضعیف، مسیرهای آب زیرزمینی و اختلالات ناشی از معدنکاری با هم در تعامل هستند. این مطالعه، بازسازی مهندسی-زمین‌شناسی مبتنی بر شواهد پنج فروچاله فروریخته را که در نزدیکی معدن پلی‌متالیک خاندیزا در جنوب ازبکستان طی سال‌های ۲۰۱۶ تا ۲۰۱۸ ایجاد شده‌اند، ارائه می‌دهد. این تجزیه و تحلیل، سوابق نقشه‌برداری زیرزمینی و سطحی، کلاس‌های فاصله گسل، داده‌های مقاومت آزمایشگاهی، مشاهدات تغییر شکل وابسته به زمان بایگانی شده، شواهد هیدروژئولوژیکی، اطلاعات توسعه معدن و اندازه‌گیری‌های میدانی مکرر از منطقه فروریخته را ادغام می‌کند. ضریب خلأ شکستگی بایگانی شده (یک شاخص مهندسی مقایسه‌ای متمایز از تخلخل ماتریس) از ۱.۵ تا ۳.۰٪ در ۱۵ تا ۲۰ متر از گسل‌های اصلی به ۴.۵ تا ۸.۰٪ در منطقه گسل و کمربند نفوذ فوری آن افزایش می‌یابد، در حالی که مقاومت فشاری تک محوری از ۵ تا ۱۰ مگاپاسکال به کمتر از ۱ تا ۳ مگاپاسکال کاهش می‌یابد. در ۲۸ رکورد مقاومت برشی آزمایشگاهی، میانگین چسبندگی ۱۶.۸۳ ± ۴.۸۱ مگاپاسکال (محدوده ۷.۱ تا ۲۷.۰ مگاپاسکال) و میانگین زاویه اصطکاک داخلی ۴۲.۰۵ ± ۲.۶۳ درجه (محدوده ۳۶ تا ۴۷ درجه) است؛ این مقادیر در مقیاس نمونه هستند و به عنوان مقاومت توده سنگ یا سطح گسل درجا در نظر گرفته نمی‌شوند. پنج فروچاله به ابعاد تقریبی ۱۲ × ۱۳ تا ۶۰ × ۸۰ متر و عمق قابل مشاهده ۶ تا ۴۰ متر رسیدند. مشاهدات بایگانی شده، ناحیه تغییر شکل یافته‌ای در حدود ۰.۸ کیلومتر مربع و نرخ گسترش یا نشست ترک‌های محلی تا ۱ تا ۲ میلی‌متر در روز را ثبت می‌کنند. قوی‌ترین شواهد برای کنترل معدن، محیط غارنشینی بدون پر شدن مجدد، ریزش تدریجی سقف، اتصال گزارش شده فروچاله ۲ به افق معدنی ۱۳۴۰ متری و ارتباط مکانی-زمانی بین استخراج زیرزمینی و تغییر شکل سطحی است. آب‌های زیرزمینی و لرزش‌های لرزه‌ای منطقه‌ای به عنوان عوامل مؤثر یا محرک در نظر گرفته می‌شوند، نه به عنوان علل مستقل و اثبات‌شده، زیرا داده‌های پیوسته فشار منفذی، جریان ورودی و شتاب محل در دسترس نیستند. بنابراین، مدل مفهومی حاصل، مکانیکی و نیمه‌کمّی است، نه یک شبیه‌سازی پیش‌بینی کالیبره‌شده.

نویسنده مسئول مکاتبات: *mukhiddinjuliev@gmail.com* (م. جولیف)